



Spectral Subsurface Scattering for Material Classification

Haejoon Lee  and Aswin C. Sankaranarayanan 

Carnegie Mellon University, Pittsburgh PA 15213, USA

Abstract. This study advances material classification using Spectral Sub-Surface Scattering (\mathcal{S}^4) measurements. While spectrum and sub-surface scattering measurements have individually been used in material classification, we argue that the strong spectral dependence of subsurface scattering lends itself to highly discriminative features. However, obtaining \mathcal{S}^4 measurements requires a time-consuming hyperspectral scan. We avoid this by showing that a carefully chosen 2D projection of the \mathcal{S}^4 point spread function is sufficient for material estimation. We also design and implement a novel imaging setup, consisting of a point illumination and a spectrally-dispersing camera, to make the desired 2D projections. Finally, through comprehensive experiments, we demonstrate the superiority of \mathcal{S}^4 imaging over spectral and sub-surface scattering measurements for the task of material classification.

Keywords: Spectral Subsurface Scattering · Material Classification

1 Introduction

Identifying the material composition of an object or a scene has been an enduring challenge across numerous scientific disciplines. One approach, rooted in the early work of Newton, Fraunhofer, and many others, harnesses spectrum variations in the light reflected from objects. Since materials often have distinct spectral absorption profiles, spectral analysis of reflectance has become indispensable in inspecting materials with various scales: common daily objects such as powders [28, 47] and foods [29, 44], geographical material distribution [9, 19, 22], and the composition of celestial objects [18, 36]. Light transport in a scene, however, extends well beyond reflection. When an object is illuminated, it is not only reflected off the illuminated points but often penetrates the surface. This phenomenon, called “subsurface scattering”, is central to the appearance of objects as we perceive them, and has garnered widespread attention in a number of applications including light transport modeling [45], inverse light transport [5], scene analysis [30] and material classification [6, 26, 38, 40, 41]. Notably, subsurface scattering is also significantly influenced by the wavelength of the incident light. This strong synergy between spectral characteristics and subsurface scattering offers a unique opportunity for enhancing material classification.

Perhaps, the most informative physical measurements for understanding light transport with subsurface scattering is the spectral bidirectional scattering reflectance distribution function (BSSRDF) [45]. As such, measurement of the

BSSRDF data is impractical due to its high dimensionality and the resulting acquisition time; this gets all the more challenging when we seek to resolve it across the spectrum. To simplify this process, we reduce the complexity by omitting the angular dimension of light. Instead, we aim to measure spectral variations of subsurface scattering observed on the surface of the material. To acquire this, we assume the object’s material composition is homogeneous and illuminate it at a single point. A hyperspectral image (HSI) of this scene is subsequently acquired by sequentially scanning it with narrowband spectral filters. This approach, which we refer to as *multishot* Spectral Sub-Surface Scattering (\mathcal{S}^4) measurement, offers a more efficient way to gather the necessary data. However, the method is still limited by the need for multiple images as well as the need for a hyperspectral camera with significant spectral resolution.

To further simplify our imaging instrument, we introduce a *single-shot* \mathcal{S}^4 measurement. As before, we illuminate the scene with a point light source. We use an optical element (a grism [1] in our setup) to spectrally disperse light along one dimension; this provides us with a linear projection of the measurements made by the multishot \mathcal{S}^4 system. This single-shot approach is a significant improvement over the conventional multispectral approach, which requires complex alignment-sensitive components with predetermined spatial and spectral parameters.

Contributions. Our contributions to advancing material classification:

- We formulate material classification using spectral subsurface scattering measurements, an approach that seeks to leverage the complementary strengths of the individual modalities.
- We present a single-shot \mathcal{S}^4 imaging prototype in a laboratory setting. Our setup uses a spectral disperser and a monochrome camera to capture a single image of the backscattered light from the subsurface layers of materials illuminated by a point light source.
- Our single-shot technique is quite effective in recovering parameters describing \mathcal{S}^4 , under a physics-based model, across a wide range of materials.
- We provide a thorough analysis of the efficacy of our \mathcal{S}^4 imaging across diverse datasets, demonstrating its versatility and robustness.

The result is a significant enhancement in material classification, surpassing traditional methods based solely on spectral reflectance or broadband scattering. The code and data associated with this work can be found on the project website [24].

Limitations. Despite its promising capabilities, our single-shot \mathcal{S}^4 imaging method faces several challenges. It necessitates an active illumination setup, which may not be practical in environments where lighting cannot be controlled. The system’s accuracy is dependent on the object’s surface geometry; non-uniform or irregular surfaces could disrupt the uniformity of the spectral scattering kernel, leading to classification errors. Additionally, the technique’s ability to probe subsurface features is inherently limited by the material’s opacity and thickness. These limitations underscore the need for further refinement to enhance the method’s robustness and versatility in real-world conditions.

2 Prior Work

In this section, we briefly discuss techniques commonly used for material classification in the computer vision community.

Spectrum-based material classification. Spectral analysis evaluates optical and electronic properties such as band gap energy, extinction coefficient, and refractive index [37] and can be categorized into two approaches. The first approach is capturing images beyond the visible spectrum. In addition to using an RGB camera, capturing images in the longer wavelengths such as Near Infrared (NIR) [25, 35] and Shortwave Infrared (SWIR) spectrum [47] has been widely used. However, this approach does not have enough spectral diversity, due to the large bandwidths of filters used. The second approach captures images at higher spectral resolution using a hyperspectral camera; this has found applications in inspecting printed circuit boards [20], remotely sensing the urban surface materials [9, 19, 22], and space surveillance [18, 36]. In this work, we go beyond the spectrum by considering sub-surface scattering in tandem.

Sub-surface scattering and material classification. Subsurface scattering information has also been pivotal in material classification. Light scattering can provide information about the structural characteristics of the material such as variations of particle number density with radius [7]. For instance, Steimle *et al.* [38] and Mao *et al.* [26] actively projected a dot pattern and captured the backscattered light to classify materials. However, these methods only look at monochrome images. A different approach is to use a time-of-flight (ToF) camera [6, 39–41] to capture the temporal point spread function, which is affected by the extent of subsurface scattering. However, due to the multipath interference in ToF cameras, these methods exhibit limited robustness against geometric variations.

Hyperspectral subsurface scattering. Hyperspectral scattering imaging has proven to be beneficial in agriculture and food research communities by providing detailed insights into the physical properties of biological materials, which show strong scattering signals. This method has been instrumental in assessing fruit quality by correlating spectral scattering profiles with firmness and soluble solids content [32], predicting meat tenderness with high precision in the food industry [46], and determining the bulk density and particle size in wheat flour [48], thereby enhancing quality control measures in agriculture and food production. However, hyperspectral imaging is time-consuming, which is not ideal for many applications. We resolve this with our single-shot \mathcal{S}^4 design.

Hyperspectral imaging. The design of classical hyperspectral cameras is based on scanning—either in space as with the push broom device or in the spectrum as in tunable filters. This sequential scanning is time-consuming as well as light inefficient. Many designs have been proposed to overcome these limitations including mosaic cameras [14], spectral scanning [23], spatio-spectral scanning [33],

compressive imaging [42], computed tomography imaging [21], and prism-mask systems [2], each with its own relative merits. Our single-shot \mathcal{S}^4 imaging system is inspired by these designs.

3 Spectral Subsurface Scattering Imaging

In this section, we present the Farrell model for spectral subsurface light transport and introduce our multishot and single-shot \mathcal{S}^4 imaging systems.

3.1 The Farrell Model for Spectral Subsurface Light Transport.

A comprehensive treatment of light transport within a scattering media is provided by the Radiative Transport Equation (RTE), which describes $L(\mathbf{x}, \boldsymbol{\omega})$, the radiance at a point \mathbf{x} in direction $\boldsymbol{\omega}$, in terms of the material's extinction coefficient σ_t , scattering coefficient σ_s , and its phase function p [4]:

$$(\boldsymbol{\omega} \cdot \nabla)L(\mathbf{x}, \boldsymbol{\omega}) = -\sigma_t L(\mathbf{x}, \boldsymbol{\omega}) + \sigma_s \int_{4\pi} p(\boldsymbol{\omega}, \boldsymbol{\omega}') L(\mathbf{x}, \boldsymbol{\omega}') d\boldsymbol{\omega}'. \quad (1)$$

In scenarios where scattering is predominant, light transport described by the RTE can be approximated as a diffusion process for which analytical solutions can be derived in certain scenarios. For instance, Farrell *et al.* [12] investigated the diffuse reflectance for the surface of a semi-infinite homogeneous medium upon being illuminated by a vertically oriented, infinitesimally small light source. They derived an analytical solution to describe the diffuse reflectance, R_f , which is the portion of the incident light remitted out of the upper boundary at each point at the surface of the medium [43]:

$$R_f(r) = \frac{a'}{4\pi} \left[\frac{1}{\sigma'_t} \left(\sigma_{\text{eff}} + \frac{1}{r_1} \right) \frac{\exp(-\sigma_{\text{eff}} r_1)}{r_1^2} + \left(\frac{1}{\sigma'_t} + \frac{4A}{3\sigma'_t} \right) \left(\sigma_{\text{eff}} + \frac{1}{r_2} \right) \frac{\exp(-\sigma_{\text{eff}} r_2)}{r_2^2} \right], \quad (2)$$

where r is the distance from the incident point, a' is the transport albedo defined as $a' = \sigma'_s / (\sigma_a + \sigma'_s)$. σ_{eff} is the effective attenuation coefficient given by $\sigma_{\text{eff}} = [3\sigma_a(\sigma_a + \sigma'_s)]^{1/2}$, and σ'_t is the total interaction coefficient ($\sigma'_t = \sigma_a + \sigma'_s$). r_1 and r_2 are given by:

$$r_1 = \sqrt{\left(\frac{1}{\sigma'_t} \right)^2 + r^2}, \quad r_2 = \sqrt{\left(\frac{1}{\sigma'_t} + \frac{4A}{3\sigma'_t} \right)^2 + r^2}. \quad (3)$$

Here, A represents the internal reflection coefficient, which is determined by the refractive index mismatch at the interface and can be calculated using empirical equations [16]. It is important to note that every parameter in Eq. (2) except r for r_1 and r_2 is dependent on the wavelength of the incident light.

The Farrell model has been extensively adopted for modeling subsurface light transport in graphics [10, 45] and estimating optical properties, such as the absorption and scattering coefficients, σ_a and σ'_s , of various scattering materials [3, 11, 15, 31]. Since σ'_s , σ_a , and A are all functions of the incident light's wavelength, $R_f(r)$ is a function of spectrum. Figure 1 shows the multispectral diffuse reflectance of a scattering medium captured with our imaging setup.

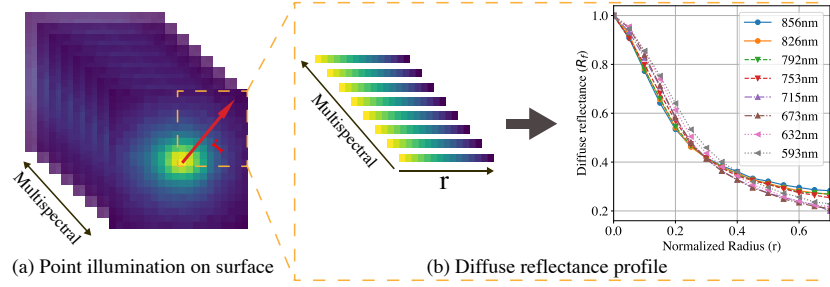


Fig. 1: Multispectral diffuse reflectance profile of a scattering medium measured with our setup. (a) Captured multispectral image of backscattered point illumination on the surface of subject material, (b) Diffuse reflectance profile computed by taking intensity values from illumination center toward outside. As shown in the right side plot, the profile is also a function of the wavelength of the incident light.

3.2 Multishot \mathcal{S}^4 Imaging System

The multishot \mathcal{S}^4 imaging setup comprises a light source, a camera, and a tunable bandpass spectral filter. We sequentially scan the illuminated surface with the tunable filter to obtain a 16-channel multispectral scattering image. The measurements of the i -th channel at pixel (x, y) from the multishot setup can be expressed as follows:

$$k_m(x, y, i) = \int_{\lambda \in \mathcal{C}^i} k(x, y, \lambda) d\lambda, \quad (4)$$

where $k(x, y, \lambda)$ is the spectral subsurface scattering kernel at wavelength λ , and \mathcal{C}^i denotes the bandwidth of the i -th channel.

Implementation details. Figure 2 illustrates the laboratory prototype of the multishot \mathcal{S}^4 imaging system. This setup combines a point light source, a monochrome camera that captures near-infrared (NIR) light (Hamamatsu ORCA Flash 4.0 LT), and a tunable spectral filter. The tunable filter is two Continuously Variable Filters (CVFs), which are specialized edge-pass spectral filters whose cut-off wavelength varies continuously along one axis [8]; we use two of them: one long-pass and one short-pass. By juxtaposing the long-pass and short-pass filters, we can create a linearly-varying bandpass filter, with the bandwidth determined by the relative displacement between the two, and a center wavelength that varies continuously along the filter. The illustration of CVBF is shown in Figure 2. We can then fine-tune the spectral selection by precisely adjusting the placement of these CVBF with respect to the camera using motorized translation stages. This arrangement allows us to capture images across 16 distinct spectral channels, with the bandwidth of each channel depicted in Fig. 2. For both multi- and single-shot systems (which we describe next), a point light source was projected onto the surface of a sample (see Fig. 4), creating an impulse illumination on the scene.

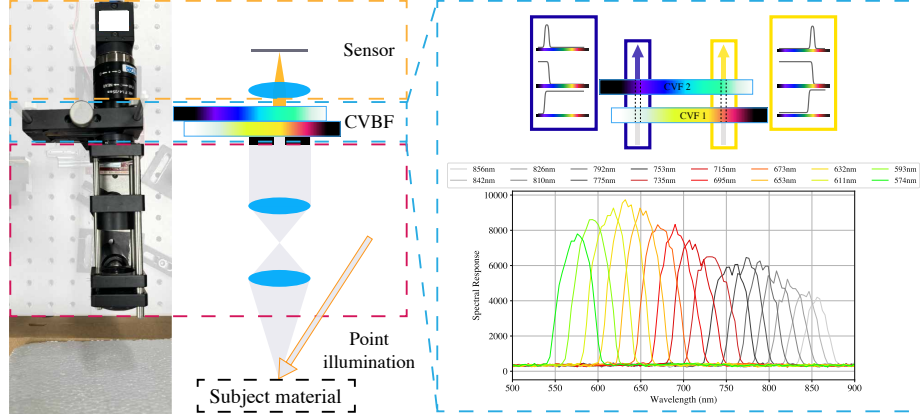


Fig. 2: The multishot \mathcal{S}^4 imaging setup, showing our laboratory prototype and its schematic representation on the left. The Continuously Variable Bandpass Filter (CVBF), depicted on the right, features a spatially varying central wavelength of narrowband. It enables the acquisition of 16-channel multispectral scattering images by sequentially shifting the CVBF across the camera lens. The spectral bandwidths for the 16 channels, measured using a spectrometer, are shown in the lower right corner.

3.3 \mathcal{S}^4 Single-shot Imaging System

Multispectral imaging techniques are complex, comprising multiple alignment-sensitive components with predetermined spatial and spectral parameters [34]. Especially, multishot approaches require long exposure times to capture narrowband spectral images. To address this issue, we propose a single-shot \mathcal{S}^4 imaging method that further simplifies the capture setup.

The key idea of single-shot \mathcal{S}^4 imaging is capturing scattering images through a spectral disperser, which spatially disperses the scattering kernel in each wavelength, as illustrated in Fig. 3. The dispersed scattering kernel captured through the single-shot \mathcal{S}^4 imaging setup can be expressed as:

$$k_s(x, y) = \int_{\lambda} k(x - \delta(\lambda - \lambda_c), y, \lambda) d\lambda, \quad (5)$$

where δ is the dispersion coefficient of the spectral disperser, and λ_c is the central wavelength of the spectral disperser.

Figure 5 presents the prototype of the single-shot \mathcal{S}^4 imaging system. The system incorporates a point light source, a monochrome camera sensitive to near-infrared (NIR) light (Hamamatsu ORCA Flash 4.0 LT), and a spectral dispersing element, which is a grism. We built the point light source by placing a stainless

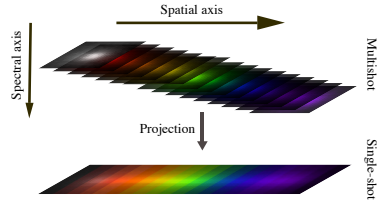


Fig. 3: Multishot and single-shot \mathcal{S}^4 imaging measurements.

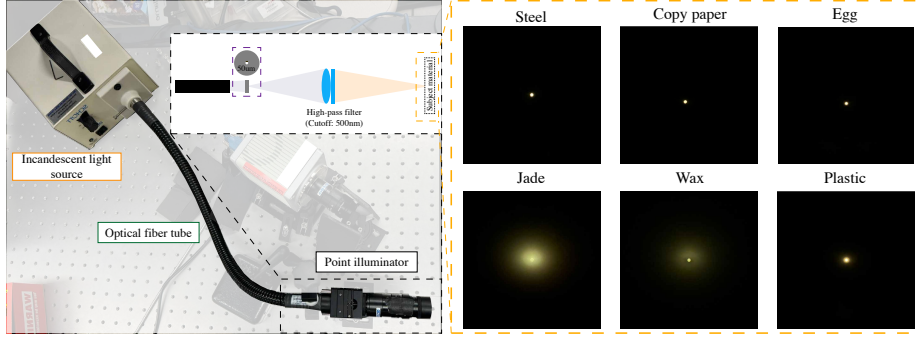


Fig. 4: Point illumination. An image of our laboratory prototype on the right side, and images of the point illumination on the surface of a few samples on the left side. The point illumination is achieved by focusing the incandescent light source onto the surface of the sample using a lens and a pinhole. For our single-shot technique, we also added a high-pass filter with a cutoff frequency of 500nm to avoid the overlap with the higher-order diffraction mode.

steel mask with a pinhole in front of a tube of incandescent white light source. Then the illumination was focused onto the surface of the sample using a lens.

For the spectral disperser, we use a grism, a combination of prism and grating that allows a chosen wavelength to go through undeflected. This gave us significant improvements in being able to focus correctly on the target samples. Our configuration uses a right-angle prism with an apex angle of 30° and a diffraction grating with 300 lines per millimeter. The details of the grism design and its effectiveness are elaborated in Appendix B.

Examples of the images acquired by our single-shot setup are shown in Fig. 5. The horizontal bars in the acquired image show the spectrally varying spatially dispersed scattering kernels, which we extract with a patch of 1200×2048 pixels; this is subsequently used for material classification as a single data sample.

4 Experiment

We present the experimental results, starting with an evaluation of the single-shot model and subsequently its effectiveness in material classification.

4.1 Justification of Single-Shot \mathcal{S}^4 Imaging

Before delving into material classification with our single-shot approach, we aim to demonstrate its feasibility. Specifically, we fit the Farrell model on the measurements made with the multishot \mathcal{S}^4 imaging setup and compare the model parameters to those fit on a simulated single-shot setup on the multishot data. We provide the details of the model fitting in Appendix C, summarizing the conclusions here.

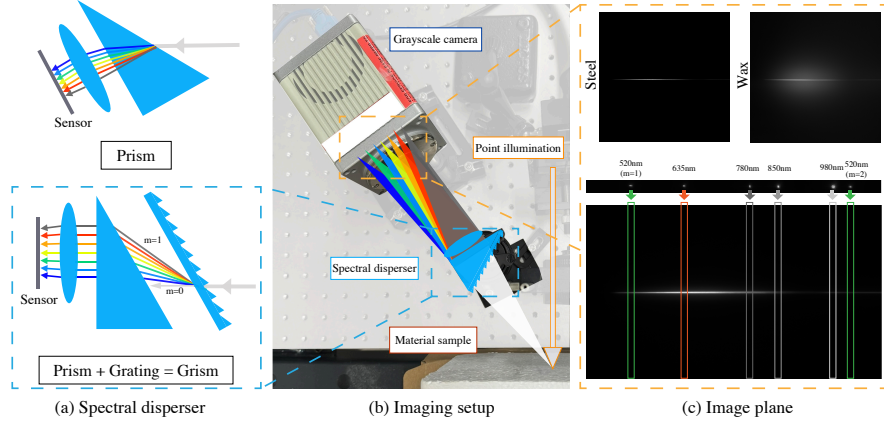


Fig. 5: Single-shot \mathcal{S}^4 imaging setup, featuring: (a) Schematic illustrations of spectral dispersers, including both prism and grism. The precise alignment of grating and prism facilitates a direct light path for spectral dispersion, aligning with the light’s trajectory from the scene. (b) The lab prototype of our single-shot \mathcal{S}^4 imaging system employing a grism. (c) Sample single-shot \mathcal{S}^4 images of steel and wax. Below, we depict wavelength markers derived from illuminating the subjects with monochrome lasers of distinct wavelengths, captured using our imaging system. The position of each laser spot along the row axis corresponds to its wavelength, effectively mapping the spectral dispersion.

To show that single-shot measurements are sufficient for modeling spectral subsurface scattering, we computed the distance between the diffuse reflectances from the measurements and the optimized Farrell models. The comparative analysis of the distance is illustrated in Fig. 6. It is important to note that $d(R_{f,d}, R_{f,m1})$, which is the distance between the multi-shot model and the measured data, represents the minimum achievable error. Observing the results, we find that $d(R_{f,d}, R_{f,m2})$ values, that capture the distance between the single-shot and data, are sufficiently small and exhibit a comparable scale to $d(R_{f,d}, R_{f,m1})$ across all materials. This proximity in values leads us to conclude that our single-shot \mathcal{S}^4 imaging method is capable of accurately representing the diffusive reflectance model, thereby encapsulating the unique optical properties of the materials under the measurements.

4.2 Material Classification with Single-Shot \mathcal{S}^4 Imaging

Derivation of comparable measurements. From our single-shot \mathcal{S}^4 image, we can decompose the Surface Spectral reflectance (\mathcal{S}^2) and broadband Sub-Surface Scattering (\mathcal{S}^3) measurements, which have been extensively employed for material classification as discussed in Sec. 2. The \mathcal{S}^2 measurements are obtained by the projection integral of the spectral scattering kernel over the spatial axis.

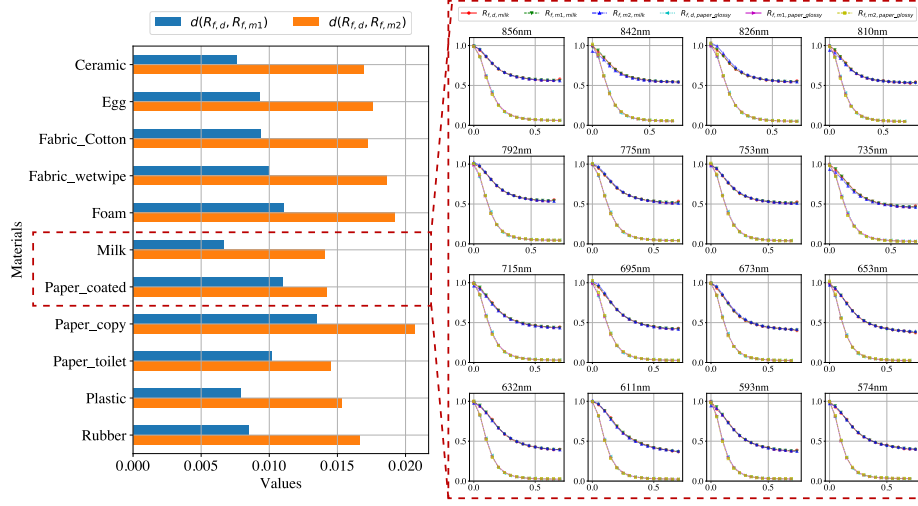


Fig. 6: Optimization results with Farrell model for multishot and simulated single-shot \mathcal{S}^4 images. The left side shows the distance between the diffuse reflectance from our dataset and the optimized Farrell models with diffuse reflectance from multishot image ($d(R_{f,d}, R_{f,m1})$), and the distance between the diffuse reflectance of dataset and optimized model with simulated single-shot image ($d(R_{f,d}, R_{f,m2})$). The right side shows both optimized Farrell models in each multispectral channel for two different materials (milk and coated paper). Despite the complexity introduced by the image dispersion operation to simulate single-shot image, we find that $d(R_{f,d}, R_{f,m2})$ values are sufficiently small and exhibit a comparable scale to $d(R_{f,d}, R_{f,m1})$ across all materials, indicating that the single-shot measurements are capable of accurately representing the diffusive reflectance.

The process could be expressed as:

$$R(\lambda) = R(x) = \int_y k_s(x, y) dy. \quad (6)$$

The size of \mathcal{S}^2 measurements derived from each \mathcal{S}^4 is 1×2048 . If the scattering kernel on each wavelength only spreads in the column axis, the \mathcal{S}^2 will be equivalent to the spectral reflectance of the surface. However, due to the spreading in the row axis (spectral axis) as well, each kernel smeared along the row axis overlapping with spectrally proximal kernels. Thus, the computed \mathcal{S}^2 measurements are expected to be blurred spectral reflectance. The \mathcal{S}^3 measurements are obtained by integrating the spectral scattering kernel over the spectral axis. The process could be expressed as:

$$k_b(r) = k_b(y) = \int_x k_s(x, y) dx. \quad (7)$$

The size of derived \mathcal{S}^3 measurements is 1200×1 . Through the operation, we can reconstruct the broadband scattering kernel before the spectral dispersion from



Fig. 7: Sample images from the white materials dataset.

our single-shot \mathcal{S}^4 imaging. We compare classification performance with \mathcal{S}^2 and \mathcal{S}^3 as a baseline to establish the overall effectiveness of \mathcal{S}^4 measurements.

Dataset 1: White materials. The challenge of material classification in computer vision is exacerbated by the color uniformity across diverse materials. To tackle this challenge with our proposed single-shot \mathcal{S}^4 imaging, we collected a dataset comprising 25 classes of white materials, which include a variety of substances such as ceramic, clays (plaster and soft clay), egg, cotton, various fabrics types (PET fabric, silk, and wet wipe), foam, artificial and genuine leather, milk, paint, various paper types (copy, coated, kitchen, and toilet), plastic, rubber, steel, various stone types (jade, marble, pumice stone), wax, and wood. For a robust evaluation, each material class contains three distinct items (for instance, the plastic class includes a food container, a bottle, and a cosmetic container). This approach facilitates three-fold cross-validation, with each fold scanning a distinct set of 25 objects across separate days to reduce data correlation between training and test sets. Every object underwent five scans on different surface areas. Fig. 7 showcases sample images of individual items from each material class within our dataset.

In Fig. 8, we illustrate the radii of spectral scattering kernels for the whole dataset (75 objects). It was computed by analyzing every column of our single-shot \mathcal{S}^4 image, which indicates one axis of scattering kernels dispersed along the spectral domain. The radius is defined as the distance from the peak value to the point where the scattering kernel reaches 0.1 of its maximum value. As shown in the figure, each material class has a distinct range of scattering radius values, varying across the wavelength. This observation underscores the potential of spectral scattering radius as a discriminative feature for material classification.

Classifier. While various classifiers are capable of assessing the informativeness of each measurement, it is preferable to utilize classifiers that efficiently handle non-linear data. Consequently, we opted to implement an SVM with an RBF

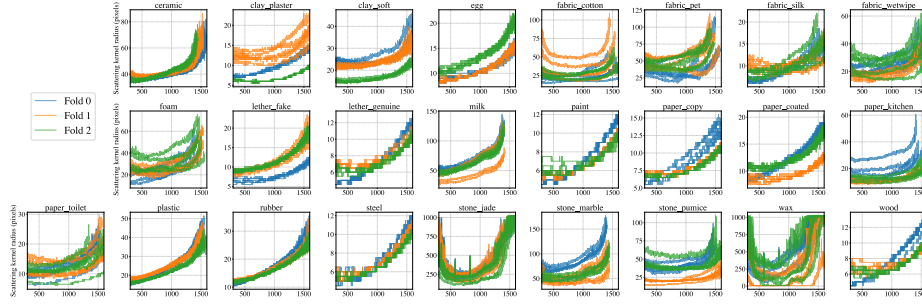


Fig. 8: Spectral scattering radii for the white materials dataset. The radius is computed by analyzing every column of the single-shot \mathcal{S}^4 image. We defined radius as the pixel distance from the peak value of each column to the point where the scattering kernel reaches 0.1 of its maximum value. This allows us to understand materials more intuitively. For example, wax and stone-jade have significantly higher scattering.

kernel, MLP, and CNN. Since \mathcal{S}^2 , \mathcal{S}^3 , and \mathcal{S}^4 data have all different dimensionality, we transform each of them to have all the same dimensions for fair comparison. For SVM and MLP, we applied PCA for the three measurements. The number of components was chosen to preserve 100% of the original data’s variance, resulting in 375 dimensions which is the same number of total data points. For CNN, we resized the \mathcal{S}^2 and \mathcal{S}^3 data to the same size as \mathcal{S}^4 image by copying and pasting the 1-dimensional data onto the row and column axis.

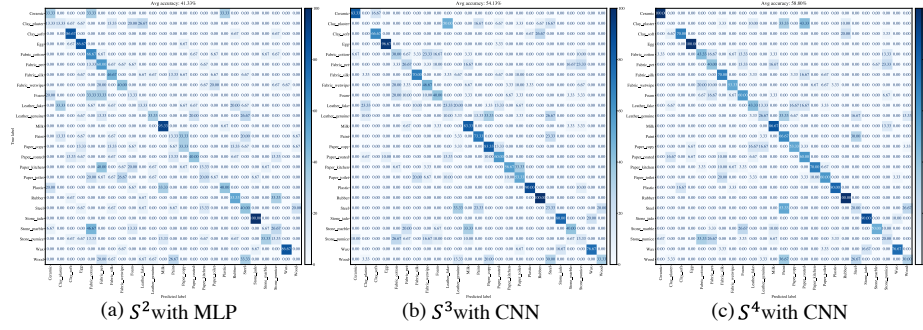
Evaluation 1: Classification. Table 1 showcases the averaged classification accuracies from a 3-fold cross-validation. Notably, the classification accuracy when utilizing \mathcal{S}^4 data reached the highest at 58.80% with CNN, outperforming the best accuracies achieved with \mathcal{S}^2 and \mathcal{S}^3 data, which were 54.13% and 41.33%, respectively. This disparity in performance underscores the superior efficacy of \mathcal{S}^4 data in material classification tasks over \mathcal{S}^2 and \mathcal{S}^3 data.

Further insights are provided in Fig. 9, which depicts the summed confusion matrix from the 3-fold cross-validation of the three measurements. Interestingly, the confusion matrices for \mathcal{S}^4 and \mathcal{S}^3 data exhibit similar patterns, with the matrix for \mathcal{S}^4 data displaying a more pronounced diagonal trend, indicating higher classification accuracy. Conversely, the confusion matrix for \mathcal{S}^2 data reveals a slightly different pattern. For instance, the classification of ‘rubber’ achieved notable accuracies of 100% with \mathcal{S}^4 and \mathcal{S}^3 data, respectively, contrasted by a mere 53.33% accuracy when using \mathcal{S}^2 data. Meanwhile, the highest classification accuracy of ‘Clay_soft’ was achieved with \mathcal{S}^2 data, at 86.67%, compared to 66.67% and 70.00% with \mathcal{S}^3 and \mathcal{S}^4 data, respectively.

An additional observation is the frequent misclassification among certain classes within broader categories, such as fabrics and papers. This trend is reflective of the inherent challenge in distinguishing materials with closely related material properties. In our dataset, some materials naturally exhibit a white hue, while others have been artificially colored using paint—for instance, leathers,

Table 1: Averaged classification accuracy from 3-fold cross-validation for surface spectral (\mathcal{S}^2), sub-surface scattering (\mathcal{S}^3), and \mathcal{S}^4 with different classifiers.

	\mathcal{S}^2 (S. Reflectance)	\mathcal{S}^3 (B. Scattering)	\mathcal{S}^4 (S. Scattering)
SVM	40.53%	46.93%	52.27%
MLP	<u>41.33%</u>	52.53%	55.20%
CNN	35.47%	<u>54.13%</u>	<u>58.80%</u>

**Fig. 9:** Confusion matrix summed from 3-fold cross-validation results for \mathcal{S}^2 , \mathcal{S}^3 , and \mathcal{S}^4 with best classifiers.

steel, and wood. We observed that these painted objects were frequently misclassified from each other. This highlights the effectiveness of our method to analyze the surface of materials, while the complexity of accurately classifying materials that are coated or covered with substances such as paint.

Dataset 2: Black coffee with different concentrations. After assessing our imaging setup on white, solid materials through a classification task, we proceeded to explore a distinctly different dataset and task. We assembled a dataset of black coffee at various concentrations to tackle a regression problem. The experiment began with 80 ml (approximately 1/3 cup) of pure water in a transparent bottle, to which we incrementally added 0.63 ml (about 1/8 tsp) of instant coffee powder, repeating this addition 10 times. This process resulted in 10 distinct labels of coffee concentrations. For each concentration class, we made two separate bottles to avoid correlation, capturing their images at different times. This approach allowed us to perform a 2-fold cross-validation. We scanned each class five times, focusing on different surface areas of the bottles each time.

Evaluation 2: Regression. For the regression task, we employed three different models: Random Forest, Ridge, and MLP. The results are summarized in Tab. 2. The Ridge and MLP models achieved the lowest Mean Squared Error (MSE) for \mathcal{S}^2 , \mathcal{S}^3 , and \mathcal{S}^4 data, with the MLP model outperforming the Ridge model in the \mathcal{S}^3 and \mathcal{S}^4 datasets. Compared to the first experiment, \mathcal{S}^4

Table 2: Averaged MSE from 2-fold cross-validation for \mathcal{S}^2 , \mathcal{S}^3 , and \mathcal{S}^4 data with different regression models.

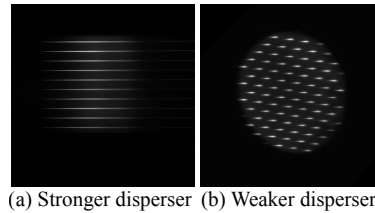
	\mathcal{S}^2	\mathcal{S}^3	\mathcal{S}^4
Random Forest	8.18	4.54	11.33
Ridge	<u>5.09</u>	3.13	3.09
MLP	5.15	<u>1.78</u>	<u>1.73</u>

and \mathcal{S}^3 results greatly outperformed \mathcal{S}^2 results, producing a small gap between each other with the best regression model, MLP. Since our dataset comprises the equivalent medium (water) with only a difference in concentration of participating particles (coffee powder), the information on the coffee concentration is expected to be more related to the broadband scattering information than the spectral information.

5 Discussion

This study presents a novel approach to material classification by leveraging single-shot \mathcal{S}^4 imaging. We have demonstrated the feasibility of the single-shot approach by comparing the scattering models estimated from them to those from the multishot technique. Then, we conducted material classification with the comprehensive datasets, which showed that our single-shot \mathcal{S}^4 outperformed measurements of the traditional approach, which are spectrum and sub-surface scattering in isolation, in distinguishing materials.

Multi-material classification. Although we only present a single spectral scattering kernel image per material, our method is not necessarily limited to a single material. Our measurements are based on a single-point illumination on the surface, so we can handle more complex scenes by illuminating multiple points on the scene and classifying each in isolation. We provide examples of imaging taken with our single-shot \mathcal{S}^4 imaging using point array illumination in Fig. 10 (a) and (b). However, the number of such points we can illuminate on a scene depends on the size of the \mathcal{S}^4 kernel, and there is an inherent tradeoff between the size of the spectral kernel and the number of illuminated points.

**Fig. 10:** Multipoint illumination for multi-material classification.

Challenges and limitations. Despite its promising capabilities, the single-shot \mathcal{S}^4 imaging method faces several challenges. The requirement for active illumination and the dependence on surface geometry to be smooth are limitations that may restrict the method’s applicability in uncontrolled environments. Additionally,

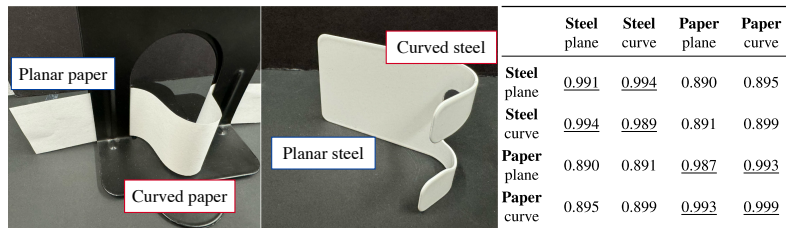


Fig. 11: (Left) two material samples we scanned that have planar and curved surfaces. We collected two measurements per surface and per material. (right) Average normalized cross-correlation between the different types of surfaces, showing inter- and intra-class consistency across curvatures. This suggests that the \mathcal{S}^4 measurements are stable despite changes in surface geometry.

the technique’s effectiveness is inherently limited by the material’s opacity, with opaque materials reducing the informativeness of \mathcal{S}^4 measurements.

Non-uniform or irregular surfaces lead to unmodelled variations in the scattering kernel across different surface areas, impacting the consistency of measurements. As illustrated in Fig. 8, materials with non-uniform surfaces, such as cotton and kitchen paper, exhibit significant changes in the scattering kernel’s radius at different locations within the same object (or fold). Such variability can adversely influence the classification accuracy of our technique. However, most objects in daily life have planar or smoothly curved surfaces. To check the robustness of our method to such surface variations, we empirically measured their actual effect by looking at two materials: copy paper, which can be naturally shaped, and steel, where the object we used had a curved contour (Fig. 11). The \mathcal{S}^4 measurements between the planar and curved counterparts show remarkable similarity with high cross-correlation values, indicating some tolerance to surface geometry.

The efficacy of our single-shot \mathcal{S}^4 imaging in accurately capturing the scattering kernel across wavelengths is affected by the scattering kernel’s size. Our setup utilizes a spectral disperser, which generates a continuous dispersion of spectral scattering kernels. Consequently, larger scattering kernels, like those observed with ‘stone_jade’ and ‘wax’ in Fig. 8 result in extensive overlapping of scattering kernels. This overlap reduces the spectral domain’s informativeness, rendering it nearly equivalent to broadband subsurface scattering.

Conclusion. Our single-shot \mathcal{S}^4 imaging presents a new modality for material classification. By harnessing the power of spectral subsurface scattering, it offers a more detailed analysis of materials, surpassing the capabilities of traditional measurements. Despite its current limitations, the method’s potential applications in various fields—from robot vision to food assessment—underscore its importance in advancing various areas that accommodate computer vision techniques. As we continue to refine and expand this technology, we hope it will play a pivotal role in material analysis and classification.

Acknowledgements

This work was supported in part by the National Geospatial-Intelligence Agency's Academic Research Program (Grant# HM0476-22-1-0004). The views expressed in this paper do not necessarily reflect those of the National Geospatial-Intelligence Agency, the Department of Defense, or any other department or agency of the US Government. The authors were also supported in part by a Sony Faculty Innovation Award, a grant from the Commonwealth of Pennsylvania, Department of Community and Economic Development, and a TCS Presidential Fellowship. The authors thank collaborators at Sony Corp., specifically, Ryuichi Tadano, Tuo Zhuang, Koya Kobayashi, Ilya Reshetouski, Hideki Oyaizu, and Jun Murayama, for valuable discussions leading to this work.

References

1. Grism (wikipedia article). <https://en.wikipedia.org/wiki/Grism>
2. Cao, X., Du, H., Tong, X., Dai, Q., Lin, S.: A prism-mask system for multispectral video acquisition. *IEEE Trans. Pattern Anal. Mach. Intell.* **33**(12), 2423–2435 (2011)
3. Cen, H., Lu, R., Dolan, K.: Optimization of inverse algorithm for estimating the optical properties of biological materials using spatially-resolved diffuse reflectance. *Inverse Problems in Science and Engineering* **18**(6), 853–872 (2010)
4. Chandrasekhar, S.: Radiative transfer. Courier Corporation (2013)
5. Che, C., Luan, F., Zhao, S., Bala, K., Gkioulekas, I.: Towards learning-based inverse subsurface scattering. In: *IEEE Int. Conf. Comput. Photography (ICCP)*. pp. 1–12 (2020)
6. Conde, M.H.: A material-sensing time-of-flight camera. *IEEE Sens. Lett.* **4**(7), 1–4 (2020)
7. Dave, J.: Determination of size distribution of spherical polydispersions using scattered radiation data. *Applied Optics* **10**(9), 2035–2044 (1971)
8. Delta Optical Thin Film A/S: Continuously Variable Filters. <https://deltaopticalthinfilm.com/products/continuously-variable-filters/>
9. Deshpande, S., Inamdar, A., Vin, H.: Spectral library and discrimination analysis of indian urban materials. *J. Indian Soc. Remote Sens.* **47**, 867–877 (2019)
10. Donner, C., Jensen, H.W.: Light diffusion in multi-layered translucent materials. *ACM Trans. Graph.* **24**(3), 1032–1039 (2005)
11. Doornbos, R., Lang, R., Aalders, M., Cross, F., Sterenborg, H.: The determination of in vivo human tissue optical properties and absolute chromophore concentrations using spatially resolved steady-state diffuse reflectance spectroscopy. *Physics in Medicine & Biology* **44**(4), 967 (1999)
12. Farrell, T.J., Patterson, M.S., Wilson, B.: A diffusion theory model of spatially resolved, steady-state diffuse reflectance for the noninvasive determination of tissue optical properties in vivo. *Medical Physics* **19**(4), 879–888 (1992)
13. Frisvad, J.R., Christensen, N.J., Jensen, H.W.: Computing the scattering properties of participating media using lorenz-mie theory. In: *ACM Trans. Graph. (Proc. SIGGRAPH)*, pp. 60–es (2007)
14. Geelen, B., Blanch, C., Gonzalez, P., Tack, N., Lambrechts, A.: A tiny vis-nir snapshot multispectral camera. In: *Adv. Fabric. Technol. Micro/Nano Opt. Photon. VIII*. vol. 9374, pp. 194–201. SPIE (2015)

15. Gobin, L., Blanchot, L., Saint-Jalmes, H.: Integrating the digitized backscattered image to measure absorption and reduced-scattering coefficients in vivo. *Applied Optics* **38**(19), 4217–4227 (1999)
16. Groenhuis, R., Ferwerda, H.A., Ten Bosch, J.: Scattering and absorption of turbid materials determined from reflection measurements. 1: Theory. *Applied Optics* **22**(16), 2456–2462 (1983)
17. Hahn, D.W.: Light scattering theory. Department of Mechanical and Aerospace Engineering, University of Florida p. 18 (2009)
18. Hege, E.K., O’Connell, D., Johnson, W., Bastý, S., Dereniak, E.L.: Hyperspectral imaging for astronomy and space surveillance. In: *Imaging Spectrom. IX.* vol. 5159, pp. 380–391. SPIE (2004)
19. Heiden, U., Segl, K., Roessner, S., Kaufmann, H.: Determination of robust spectral features for identification of urban surface materials in hyperspectral remote sensing data. *Remote Sens. Environ.* **111**, 537–552 (2007)
20. Ibrahim, A., Tominaga, S., Horiuchi, T.: Material classification for printed circuit boards by spectral imaging system. In: *Computational Color Imaging: Second Int. Workshop, CCIW 2009.* pp. 216–225. Springer (2009)
21. Johnson, W.R., Wilson, D.W., Fink, W., Humayun, M., Bearman, G.: Snapshot hyperspectral imaging in ophthalmology. *J. Biomed. Opt.* **12**(1), 014036–014036 (2007)
22. Le Bris, A., Chehata, N., Briottet, X., Paparoditis, N.: Spectral band selection for urban material classification using hyperspectral libraries. In: *23. ISPRS Congress.* vol. 3, p. np (2016)
23. Lee, H., Kim, M.H.: Building a two-way hyperspectral imaging system with liquid crystal tunable filters. In: *Image Signal Process.: 6th Int. Conf., ICISP 2014.* pp. 26–34. Springer (2014)
24. Lee, Haejoon and Sankaranarayanan, Aswin C.: Spectral Subsurface Scattering for Material Classification. <https://github.com/Image-Science-Lab-cmu/S4Imaging> (2024)
25. Liang, Y., Wakaki, R., Nobuhara, S., Nishino, K.: Multimodal material segmentation. In: *Proc. IEEE/CVF Conf. Comput. Vis. Pattern Recog.* pp. 19800–19808 (2022)
26. Mao, S., Ji, M., Wang, B., Dai, Q., Fang, L.: Surface material perception through multimodal learning. *IEEE J. Sel. Topics Signal Process.* **16**(4), 843–853 (2022)
27. Mie, G.: Beiträge zur optik trüber medien, speziell kolloidaler metallösungen. *Annalen der Physik* **330**(3), 377–445 (1908)
28. Mohamed, M.Y., Solihin, M.I., Astuti, W., Ang, C., Zailah, W.: Food powders classification using handheld near-infrared spectroscopy and support vector machine. *J. Phys.: Conf. Ser.* **1367** (2019)
29. Nawrocka, A., Lamorska, J.: Determination of food quality by using spectroscopic methods. In: *Advances in Agrophysical Research.* IntechOpen (2013)
30. Nayar, S.K., Krishnan, G., Grossberg, M.D., Raskar, R.: Fast separation of direct and global components of a scene using high frequency illumination. In: *ACM Trans. Graph. (Proc. SIGGRAPH),* pp. 935–944 (2006)
31. Nichols, M.G., Hull, E.L., Foster, T.H.: Design and testing of a white-light, steady-state diffuse reflectance spectrometer for determination of optical properties of highly scattering systems. *Applied Optics* **36**(1), 93–104 (1997)
32. Peng, Y., Lu, R.: Analysis of spatially resolved hyperspectral scattering images for assessing apple fruit firmness and soluble solids content. *Postharvest Biol. Technol.* **48**(1), 52–62 (2008)

33. Pichette, J., Charle, W., Lambrechts, A.: Fast and compact internal scanning cmos-based hyperspectral camera: the snapscan. In: Photonic Instrum. Eng. IV. vol. 10110, pp. 292–301. SPIE (2017)
34. Sahoo, S.K., Tang, D., Dang, C.: Single-shot multispectral imaging with a monochromatic camera. *Optica* **4**(10), 1209–1213 (2017)
35. Salamati, N., Fredembach, C., Süssstrunk, S.: Material classification using color and nir images. In: Proc. IS&T/SID 17th Color Imaging Conf. (CIC) (2009)
36. Scholl, J.F., Hege, E.K., Hart, M., O’Connell, D., Dereniak, E.L.: Flash hyperspectral imaging of non-stellar astronomical objects. In: Mathematics of Data/Image Pattern Recognition, Compression, and Encryption with Applications XI. vol. 7075, pp. 145–156. SPIE (2008)
37. Sindhusa, S., Padma, C., Thayanithi, V.: Experimental and theoretical investigations of organic creatinium 2-chloroacetate nonlinear optical single crystal. *J. Mater. Sci.: Mater. Electron.* **32**, 6498–6510 (2021)
38. Steimle, J., Jordt, A., Maes, P.: Flexpad: highly flexible bending interactions for projected handheld displays. In: Proc. SIGCHI Conf. Human Factors Comput. Syst. pp. 237–246 (2013)
39. Su, S., Heide, F., Swanson, R., Klein, J., Callenberg, C., Hullin, M., Heidrich, W.: Material classification using raw time-of-flight measurements. In: IEEE Conf. Comput. Vis. Pattern Recog. (2016)
40. Tanaka, K., Mukaigawa, Y., Funatomi, T., Kubo, H., Matsushita, Y., Yagi, Y.: Material classification using frequency- and depth-dependent time-of-flight distortion. In: IEEE Conf. Comput. Vis. Pattern Recog. (2017)
41. Tanaka, K., Mukaigawa, Y., Funatomi, T., Kubo, H., Matsushita, Y., Yagi, Y.: Material classification from time-of-flight distortions. *IEEE Trans. Pattern Anal. Mach. Intell.* **41**(12), 2906–2918 (2019)
42. Wagadarikar, A., John, R., Willett, R., Brady, D.: Single disperser design for coded aperture snapshot spectral imaging. *Applied Optics* **47**(10), B44–B51 (2008)
43. Wang, L., Jacques, S.L., Zheng, L.: Mclm—monte carlo modeling of light transport in multi-layered tissues. *Computer Methods and Programs in Biomedicine* **47**(2), 131–146 (1995)
44. Wang, W., Paliwal, J.: Near-infrared spectroscopy and imaging in food quality and safety. *Sens. Instrum. Food Qual. Saf.* **1**, 193–207 (2007)
45. Wann Jensen, H., Marschner, S.R., Levoy, M., Hanrahan, P.: A practical model for subsurface light transport. In: Seminal Graphics Papers: Pushing the Boundaries, Volume 2, pp. 319–326 (2023)
46. Wu, J., Peng, Y., Li, Y., Wang, W., Chen, J., Dhakal, S.: Prediction of beef quality attributes using vis/nir hyperspectral scattering imaging technique. *J. Food Eng.* **109**(2), 267–273 (2012)
47. Zhi, T., Pires, B.R., Hebert, M., Narasimhan, S.G.: Multispectral imaging for fine-grained recognition of powders on complex backgrounds. In: IEEE Conf. Comput. Vis. Pattern Recog. (2019)
48. Zhu, Q., Xing, Y., Lu, R., Huang, M., Ng, P.K.: Visible/shortwave near infrared spectroscopy and hyperspectral scattering for determining bulk density and particle size of wheat flour. *J. Near Infrared Spectrosc.* **25**(2), 116–126 (2017)